Metal Transfer and Arc Plasma in Gas Metal Arc Welding

J. Hu[1]

H. L. Tsai[2]
e-mail: tsai@umr.edu

Department of Mechanical and Aerospace Engineering,
University of Missouri-Rolla,
Rolla, MO 65409

This article analyzes the transient complex heat transfer and fluid flow in molten metal and arc plasma during the gas metal arc welding process. The model predicts the formation, growth, detachment, and transfer of droplets from the tip of a continuously fed electrode under the influences of several competing forces including gravity, electromagnetic force, arc pressure, plasma shear stress, and surface tension. Simulations were conducted for five different current levels to study the effects of current on the distributions of temperature, velocity, pressure, and current density in the droplet and/or the arc plasma. Agreement between the simulated results and published experimental data was obtained. [DOI: 10.1115/1.2724847]

Keywords: gas metal arc welding, metal transfer, arc plasma, droplet formation, free surface

1 Introduction

Gas metal arc welding (GMAW) is an arc welding process that uses a plasma arc between a continuous, consumable filler-metal electrode and the weld pool, as shown in Fig. 1. The high temperature plasma arc melts the electrode and forms a droplet at the electrode tip. The droplet is detached and transferred in the arc to the workpiece. A weld pool forms under the influences of the arc plasma and the periodical impingement of droplets. In gas metal arc welding, metal transfer describes the process of the molten metal's movement from the electrode tip to the workpiece, which includes droplet formation, detachment, and transfer in the arc. The transport of droplets into the weld pool is largely responsible for the finger penetration commonly observed in the fusion zone [1]. A better understanding of the metal transfer process is important for improvements in the quality and productivity of welding. The influence of droplet impingement on the weld pool varies with the droplet size, the impingement frequency, and the impingement velocity. The welding voltage, current, arc length, shielding gas, and wire feed rate can all affect the metal transfer process [2]. Among them, current is most often studied for its influence on the droplet size, frequency, and acceleration in the arc. There are various modes of metal transfer including short-circuit, globular, spray, and streaming. Globular transfer occurs at low currents with the droplet diameter being larger than the electrode diameter. Spray transfer occurs at higher current with the droplet diameter being smaller than the electrode diameter and the droplet generation being more frequent. Experimental results [2–6] have shown that a sharp transition in the droplet detachment frequency and size occurs when the mode changes between the globular and spray transfer modes in argon shielded environment. This paper will focus on the study of the transport phenomena of globular transfer to avoid numerical error that may be caused by simulating small droplets in the spray transfer mode.

Droplet formation [6–28] has been widely investigated to obtain the droplet size and frequency under different current levels. However, many of these models [6–12] neglected the complex fluid flow and thermal phenomena during droplet formation. These models include the static force balance theory (SFBT) [7–10], magnetic pinch instability theory (PIT) [10], and the dynamic models calculating the dynamic growth of the droplet with force balance [6,11,12]. The SFBT considers the balance between gravity, axial electromagnetic force, plasma shear stress, and surface tension. The PIT considers perturbation due to the radial magnetic force acting on an infinite column of liquid metal. Recently, several numerical models have been developed to predict droplet formation and detachment by calculating the fluid flow only [13–18], heat transfer only [19], or both the fluid flow and heat transfer [20–28] in the electrode. However, the current density and heat flux distributions were assumed at the electrode surface and the arc was not included in most of the models [13–21]. Haider and Lowke [22], Haider [23–26], Zhu et al. [27], and Fan and Kovacevic [28] have included the arc in their models to predict droplet formation. However, the droplet shapes [22–27] or arc plasma distribution [27,28] obtained in those models matched experimental results [6] poorly. Droplet detachment and further acceleration in the arc were not addressed in Refs. [22–26].

Droplet acceleration in the arc has been calculated by many authors [1,21,28–31] using the empirical formulation presented by Lancaster [10]. To calculate the plasma drag force exerted on the droplet using this formulation, the droplet was assumed to have a spherical shape and was accelerated to the workpiece with a constant acceleration. The physical properties of the arc plasma, the drag coefficient, and the plasma velocity also had to be assumed. Given the range of temperature found in a welding arc, the appropriate value of the arc plasma properties is difficult to determine. There is also much uncertainty in the drag coefficient and the plasma flow velocity changes dramatically during the welding process. Furthermore, the shape of the droplet changes along the way as it is transported to the workpiece [32]. An effective method is needed to simulate droplet acceleration without assuming the droplet shape, the plasma properties, the drag coefficient, and the plasma velocity.

To accurately model the dynamic metal transfer process, the fluid flow and heat transfer in both the electrode and arc and the interaction of the droplet with the arc have to be considered. In this paper, a transient unified model, which includes the electrode, droplet, weld pool, arc, and their interactions, is developed to model the metal transfer process. The dynamic growth of the droplet at the electrode tip is simulated by integrating the heat transfer and the fluid flow in the electrode with the momentum and heat transfer from the arc. The heat flux from the arc plasma and current density distribution in the droplet are calculated in the unified model, thus no assumption of these terms need to be made as in the previous models. The changes of droplet shape and temperature, and droplet acceleration in the arc are also modeled by

[1]Present address: Department of Mechanical Engineering, University of Bridgeport, Bridgeport, CT 06604.

[2]Corresponding author.

Contributed by the Heat Transfer Division of ASME for publication in the JOURNAL OF HEAT TRANSFER. Manuscript received January 24, 2006; final manuscript received October 12, 2006. Review conducted by Ben Q. Li.

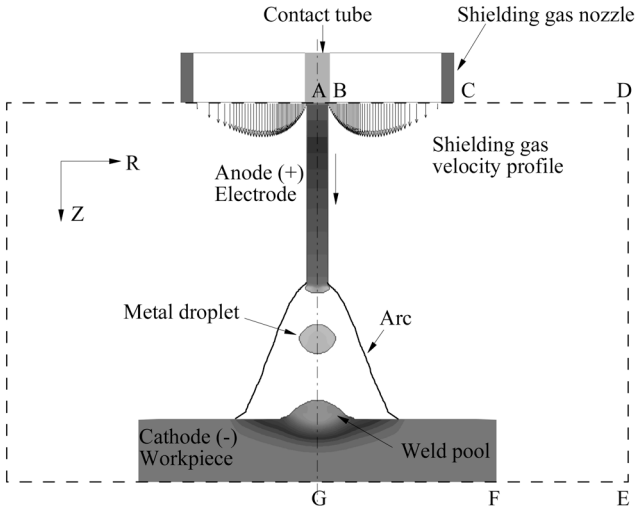

Fig. 1 A schematic representation of a GMAW system including the electrode, the arc, and the weld pool (not to scale)

simulating the fluid flow and heat transfer inside the droplet. The heat exchange between the arc and droplet and the momentum transfer from the arc to the droplet are obtained through the direct results obtained in the arc calculation at each time step. No assumptions of the arc plasma temperature, properties and velocity and the drag coefficient are needed. The simulated results are then compared with published experimental data and reasonable agreement is found.

2 Mathematical Model

2.1 Governing Equations. Figure 1 is a schematic sketch of a stationary axisymmetric GMAW system. In this system, a constant current is applied to the electrode through the contact tube at the top of the computational domain. An arc plasma is struck between the electrode and the workpiece. The electrode is continuously fed downward and then melted at the tip by the high temperature arc. Droplets are formed at the molten electrode tip, and are then detached and transferred to the workpiece. A weld pool is formed by the continuous impingement of droplets and dynamic interaction with the high temperature and high pressure arc plasma at the workpiece. Inert shielding gas is provided through the shielding gas nozzle to prevent the molten metal from oxidation.

The computational domain has an anode region, an arc region and a cathode region. For GMAW, the anode region is the electrode, and the cathode region is the workpiece. The differential equations governing the arc, the electrode, and the workpiece can be included in a single set. The differential equations governing the conservation of mass, momentum, and energy based on the continuum formulation given by Chiang and Tsai [33] are employed in the present study, and the current continuity equation is used to calculate the current density distribution. The equations are given below

Mass continuity

$$\nabla \cdot (\rho \boldsymbol{V}) = 0 \tag{1}$$

Momentum

$$\frac{\partial}{\partial t}(\rho u) + \nabla \cdot (\rho \boldsymbol{V} u) = \nabla \cdot \left(\mu_l \frac{\rho}{\rho_l} \nabla u \right) - \frac{\partial p}{\partial r} - \frac{\mu_l}{K} \frac{\rho}{\rho_l}(u - u_s) - \frac{C\rho^2}{K^{1/2}\rho_l}|u - u_s|(u - u_s) - \nabla \cdot (\rho f_s f_l \boldsymbol{V}_r u_r) - J_z \times B_\theta \tag{2}$$

$$\frac{\partial}{\partial t}(\rho v) + \nabla \cdot (\rho \boldsymbol{V} v) = \nabla \cdot \left(\mu_l \frac{\rho}{\rho_l} \nabla v \right) - \frac{\partial p}{\partial z} - \frac{\mu_l}{K} \frac{\rho}{\rho_l}(v - v_s) - \frac{C\rho^2}{K^{1/2}\rho_l}|v - v_s|(v - v_s) - \nabla \cdot (\rho f_s f_l \boldsymbol{V}_r v_r) + \rho g \beta_T (T - T_0) + J_r \times B_\theta \tag{3}$$

Energy

$$\frac{\partial}{\partial t}(\rho h) + \nabla \cdot (\rho \boldsymbol{V} h) = \nabla \cdot \left(\frac{k}{c_s} \nabla h \right) + \nabla \cdot \left(\frac{k}{c_s} \nabla (h_s - h) \right) - \nabla \cdot (\rho (\boldsymbol{V} - \boldsymbol{V}_s)(h_l - h)) - \Delta H \frac{\partial f_l}{\partial t} + \frac{J_r^2 + J_z^2}{\sigma_e} - S_R + \frac{5k_b}{e}\left(\frac{J_r}{c_s}\frac{\partial h}{\partial r} + \frac{J_z}{c_s}\frac{\partial h}{\partial z} \right) \tag{4}$$

Current continuity

$$\nabla^2 \phi = \frac{1}{r}\frac{\partial}{\partial r}\left(r \frac{\partial \phi}{\partial r} \right) + \frac{\partial^2 \phi}{\partial z^2} = 0 \tag{5}$$

Ohm's law

$$J_r = -\sigma_e \frac{\partial \phi}{\partial r} \quad J_z = -\sigma_e \frac{\partial \phi}{\partial z} \tag{6}$$

Maxwell's equation

$$B_\theta = \frac{\mu_0}{r} \int_0^r J_z r dr \tag{7}$$

In Eqs. (1)–(4), u and v are the velocities in the r and z directions, respectively. $\boldsymbol{V}_r = \boldsymbol{V}_l - \boldsymbol{V}_s$ is the relative velocity vector between the liquid phase and the solid phase in the mushy zone. The subscripts s and l refer to the solid and liquid phases, respectively, and the subscript 0 represents the initial condition. f is the mass fraction of the liquid or solid; K is the permeability function; C is the inertial coefficient; p is the pressure; T is the temperature; h is the enthalpy; Φ is the electrical potential; ρ is the density; μ is the viscosity; k is the thermal conductivity; g is the gravitational acceleration; β_T is the thermal expansion coefficient; c is the specific heat; σ_e is the electrical conductivity; J_r and J_z are current densities, in the respective r and z directions; B_θ is the self-induced electromagnetic field; S_R is the radiation heat loss; μ_0 is the magnetic permeability; k_b is the Stefan-Boltzmann constant; and e is the electronic charge.

The third and fourth terms on the right-hand side of Eqs. (2) and (3) represent the respective first- and second-order drag forces for the flow in the mushy zone. The fifth term on the right-hand side of Eqs. (2) and (3) represents an interaction between the solid and the liquid phases. The second term on the right-hand side of Eq. (4) represents the net Fourier diffusion flux. While the third term represents the energy flux associated with the relative phase motion, and the forth term is used to consider the latent heat of fusion. All the terms mentioned in this paragraph are zero, except in the mushy zone. When Eqs. (2)–(4) are used to calculate the arc plasma, these terms associated with the mushy zone are set to zero and all the thermal physical properties are replaced with those of the arc plasma. In GMAW, as the arc is concentrated, the resulting weld pool is small and the solidification time is short (relative to, for example a casting process), the solid phase velocity is as-

sumed to be zero in the present study.

The second-to-last term on the right-hand side of Eq. (3) is the thermal expansion term. The last term of Eq. (2) and Eq. (3) is the electromagnetic force term. The last three terms in Eq. (4) are Ohmic heating, radiation loss, and electron enthalpy flow, respectively.

Continuum density, specific heat, thermal conductivity, solid mass fraction, liquid mass fraction, velocity, and enthalpy are defined as follows:

$$\rho = g_s\rho_s + g_l\rho_l c = f_s c_s + f_l c_l k = g_s k_s + g_l k_l$$

$$f_s = \frac{g_s\rho_s}{\rho} \quad f_l = \frac{g_l\rho_l}{\rho}$$

$$\boldsymbol{V} = f_s\boldsymbol{V}_s + f_l\boldsymbol{V}_l \quad h = h_s f_s + h_l f_l \tag{8}$$

Assuming constant phase specific heats, the phase enthalpy for the solid and liquid can be expressed as

$$h_s = c_s T \quad h_l = c_l T + (c_s - c_l)T_s + H \tag{9}$$

where H is the latent heat of fusion for the alloy.

The assumption of permeability function in the mushy zone requires consideration of the growth morphology specific to the alloy under study. In the present study, the permeability function analogous to fluid flow in porous media is assumed, employing the Carman-Kozeny equation [34,35]

$$K = \frac{g_l^3}{c_1(1-g_l)^2} \quad c_1 = \frac{180}{d^2} \tag{10}$$

where d is proportional to the dendrite dimension, which is assumed to be a constant and is on the order of 10^{-2} cm. The inertial coefficient, C, can be calculated from [36]

$$C = 0.13 g_l^{-3/2} \tag{11}$$

2.2 Arc Region. In the arc region, the plasma is assumed to be in local thermodynamic equilibrium (LTE) [37], implying the electron and the heavy particle temperatures are equal. On this basis, the plasma properties, including enthalpy, specific heat, density, viscosity, thermal conductivity, and electrical conductivity, are determined from an equilibrium composition calculation [37]. Note the metal vaporized from the metal surface may influence plasma material properties, but this effect is omitted in the present study. It is also assumed that the plasma is optically thin, thus the radiation may be modeled in an approximate manner by defining a radiation heat loss per unit volume [37].

2.3 Anode Sheath Region. At the plasma-electrode interface, there exists an anode sheath region [37]. In this region, the mixture of plasma and metal vapor departs from LTE, thus it no longer complies with the model presented above. The anode sheath region has been neglected in many arc models [7,22,23,32], which leads to a more constricted arc distribution at the bottom of the droplet. This paper adopts the anode sheath formulation of Haidar [24] by including a noncollisional sheath region for the anode. Formulation of the noncollisional zone is based on the Langmuir sheath model. Heat transfer from the plasma to the electrode is determined by charged particle fluxes across the sheath. These fluxes are due to the electrons and the ions from the plasma, and also to a limited number of electrons emitted from the anode surface due to the thermionic emission. The corresponding current densities of these electrons and ions flow are J_e, J_i, and J_R. As J_R is several orders of magnitude lower than J_e and J_i, it is omitted in the calculation for simplification. The following formulations [24] are used to calculate the anode voltage drop across the sheath V_s

$$J = J_e - J_i$$

$$J_e = en_{e,s}\left(\frac{k_b T_{e,s}}{2\pi m_e}\right)^{0.5}\exp\left(\frac{eV_s}{k_b T_{e,s}}\right)$$

$$J_i = \tfrac{1}{4}en_{e,s}v_B$$

$$V_s \le 0 \tag{12}$$

where J is the total current density at the arc-anode interface calculated from the current density equation (5), J_i and J_e are calculated from the electron number density as charge neutrality is assumed valid through the transition zone; $T_{e,s}$ is the electron temperature at the sheath edge, which is taken as the local plasma temperature calculated from LTE; $n_{e,s}$ is the electron number density at the sheath edge, which is taken as the equilibrium electron number density at the local plasma temperature; v_B is the Bohm velocity given by $v_B=(k_b T_{e,s}/m_i)^{0.5}$; e is the electronic charge; k_b is the Stefan-Boltzmann constant; m_e is the electron mass; and m_i is the ion mass for the plasma gas.

The energy balance equation at the anode surface is modified to include a source term, S_a, expressing the heating effects due to conduction by neutral particles, charge transport across the sheath through J_e and J_i, and cooling effects due to evaporation and blackbody radiation,

$$S_a = \frac{k_{\text{eff}}(T_{e,s}-T_a)}{\delta} + J_i\left(V_i - V_s + \frac{5k_b}{2e}T_a\right) + J_e\left(\phi_w + \frac{5k_b}{2e}T_{e,s}\right) - q_{\text{ev}}H_{\text{ev}} - \epsilon k_b T_a^4 \tag{13}$$

where k_{eff} is the thermal conductivity taken at the arc plasma temperature; T_a is the anode surface temperature; δ is the mesh size adjacent to the anode surface; V_i is the ionization energy of the plasma gas; ϕ_w is the work function of the anode material; ε is the emissivity of the surface; q_{ev} is the evaporation mass rate of metal vapor, and H_{ev} is the latent heat of vaporization. For metal such as steel, q_{ev} can be written as [38]

$$\log(q_{\text{ev}}) = A_v + \log P_{\text{atm}} - 0.5\log T \tag{14}$$

$$\log P_{\text{atm}} = 6.121 - \frac{18836}{T} \tag{15}$$

The energy balance equation for the plasma in the transition zone is also modified to include a source term, S_{ap}, expressing the cooling effects due to conduction by neutral particles and charge transport across the sheath through J_e and J_i

$$S_{\text{ap}} = -\frac{k_{\text{eff}}(T_{e,s}-T_a)}{\delta} - J_i\left(V_i + \frac{5k_b}{2e}T_a\right) - J_e\left(\frac{5k_b}{2e}T_{e,s} - V_s\right) \tag{16}$$

2.4 Cathode Sheath Region. Similar to the anode region, there exists a cathode sheath region between the plasma and the cathode. However, the physics of the cathode sheath and the energy balance at the nonthermionic cathode for GMAW are not well understood [10,22–26]. The thermal effect due to the cathode sheath has been omitted in many models but reasonable results were obtained [22–26,37]. Thus, the source term of the energy balance equation at the cathode surface will only consider conduction, radiation, and evaporation

$$S_c = \frac{k_{\text{eff}}(T_{\text{arc}}-T_c)}{\delta} - q_{\text{ev}}H_{\text{ev}} - \epsilon k_b T_c^4 \tag{17}$$

where k_{eff} is the effective thermal conductivity at the arc-cathode surface taken as the thermal conductivity of the arc plasma; δ is the length of the cathode sheath region; and T_c is the cathode surface temperature.

In additional to the heat loss by conduction, another positive term is included in the energy source term for the plasma at the cathode surface. This positive term is used to approximate the

energy used in the cathode boundary layer to ionize the plasma [39] and it can also eliminate the unreasonable cooling effect of the electron flow term in the cathode region [37]. The energy source term for the plasma at the cathode surface is given by

$$S_{\mathrm{cp}} = -\frac{k_{\mathrm{eff}}(T_{\mathrm{arc}} - T_c)}{\delta} + \frac{5k_b(T_{\mathrm{arc}} - T_c)}{2e} \tag{18}$$

2.5 Metal Region (Electrode, Droplet, and Workpiece). In this model, the anode region and cathode region change their shapes with time. Together with free droplets in the arc, they consist of the metal region, which is occupied by metal. The temperature distribution within the metal region is at an energy balance of conduction, Ohmic heating, and convection in the metal and the heat transferred from the arc plasma. Considerations are also given to energy gains and losses due to latent heat resulting from melting and solidification at the solid-liquid interface. Changes in the shape of the electrode tip and the weld pool surface result in changes in the current distribution, the heat generated due to Ohmic heating, and the heat transferred from the arc to the metal surface.

2.6 Tracking of Solid-Liquid Interface. The solid/liquid phase-change boundary is handled by the continuum model [33]. The third, fourth, and fifth terms on the right-hand side of Eqs. (2) and (3) vanish at the solid phase because $u=u_s=v=v_s=0$ and $f_l=0$. For the liquid region, since K goes to infinity due to $g_l=1$ in Eq. (7) and $f_s=0$, all the aforementioned terms also vanish. These terms are only valid in the mushy zone, where $0<f_l<1$ and $0<f_s<1$. Therefore, there is no need to explicitly track the phase-change boundaries, and the liquid region, mushy zone, and solid region all are calculated by the same Eqs. (2) and (3). During the fusion and solidification processes, the latent heat is absorbed or released in the mushy zone, which is handled through the use of enthalpy defined in Eq. (9).

2.7 Tracking of Free Surfaces. Precise tracking of the free surface of the droplet and the welding pool are essential to correctly predicting the shape of the droplet and the weld pool as a function of time. The algorithm of volume-of-fluid (VOF) is used to track the moving free surface [40,41]. The fluid configuration is defined by a volume of fluid function, $F(r,z,t)$, which tracks the location of the free surface. This function represents the volume of fluid per unit volume and satisfies the following conservation equation:

$$\frac{dF}{dt} = \frac{\partial F}{\partial t} + (\boldsymbol{V}\cdot\nabla)F = 0 \tag{19}$$

When averaged over the cells of a computing mesh, the average value of F in a cell is equal to the fractional volume of the cell occupied by the metal. A unit value of F corresponds to a cell full of metal, whereas a zero value indicates the cell contains no metal. Cells with F values between zero and one are partially filled with metal.

2.8 Forces at the Arc Plasma and Metal Interface. The molten part of the metal is subjected to body forces such as gravity and electromagnetic force. It is also subjected to surface forces such as surface tension due to surface curvature, Marangoni shear stress due to temperature difference, and arc plasma shear stress and arc pressure at the arc plasma and metal interface. For cells containing a free surface, surface tension pressure normal to the free surface can be expressed as [41]

$$p_s = \gamma\kappa \tag{20}$$

where γ is the surface tension coefficient and κ is the free surface curvature given by

$$\kappa = -\left[\nabla\cdot\left(\frac{\boldsymbol{n}}{|\boldsymbol{n}|}\right)\right] = \frac{1}{|\boldsymbol{n}|}\left[\left(\frac{\boldsymbol{n}}{|\boldsymbol{n}|}\cdot\nabla\right)|\boldsymbol{n}| - (\nabla\cdot\boldsymbol{n})\right] \tag{21}$$

where $\boldsymbol{n}$ is a vector normal to the local free surface which equals the gradient of the VOF function

$$\boldsymbol{n} = \nabla F \tag{22}$$

The temperature-dependent Marangoni shear stress at the free surface in a direction tangential to the local free surface is given by [21]

$$\tau_{\mathrm{Ms}} = \frac{\partial\gamma}{\partial T}\frac{\partial T}{\partial \boldsymbol{s}} \tag{23}$$

where $\boldsymbol{s}$ is a vector tangential to the local free surface.

The arc plasma shear stress is calculated at the free surface from the velocities of arc plasma cells immediately adjacent the metal cells

$$\tau_{\mathrm{ps}} = \mu\frac{\partial \boldsymbol{V}}{\partial \boldsymbol{s}} \tag{24}$$

where μ is the viscosity of arc plasma.

The arc pressure at the metal surface is obtained from the computational result in the arc region. The surface forces are included by adding source terms to the momentum equations according to the CSF (continuum surface force) model [41,42]. Using F of the VOF function as the characteristic function, the surface tension pressure, Marangoni shear stress, arc plasma shear stress, and arc pressure are all transformed to the localized body forces and added to the momentum transport equations as source terms at the boundary cells.

2.9 Boundary Conditions

2.9.1 External Boundary Conditions. The calculation domain, as shown in Fig. 1, is ABCDEFGA. Only half of the entire physical domain is calculated due to the cylindrical symmetry along the centerline AG. The corresponding external boundary conditions for the entire domain are listed in Table 1. Symmetrical boundary conditions are used along the centerline AG. The wire feed rate is incorporated through a boundary condition on v along AB. The imposed shielding gas flow is set through a boundary condition on v along BC. For the inflow of gas from the nozzle, the radial velocity component is omitted and the axial velocity component is determined from the formula for pipe flow as shown in the following [43]:

$$v(r) = \frac{2Q}{\pi}\frac{\left\{R_n^2 - r^2 + (R_n^2 - R_w^2)\dfrac{\ln(r/R_n)}{\ln(R_n/R_w)}\right\}}{\left\{R_n^4 - R_w^4 + \dfrac{(R_n^2 - R_w^2)^2}{\ln(R_n/R_w)}\right\}} + V_w\frac{\ln\dfrac{R_n}{r}}{\ln\dfrac{R_n}{R_w}} \tag{25}$$

where Q is the inflow rate of the shielding gas, R_w is the radius of the electrode, R_n is the internal radius of the shielding gas nozzle, and V_w is the wire feed rate. A constant mass flow boundary condition is used for the open boundaries CD and DE.

The temperature boundaries along AD, DE, and EG are determined by the ambient condition, which is set as room temperature 300 K. Uniform current density is specified along AB as $J_z = -\sigma_e(\partial\phi/\partial z) = (I/\pi R_w^2)$. The voltage, ϕ, is set to zero at the bottom of the workpiece FG.

2.9.2 Internal Boundary Conditions. Within the computational domain, the moving surface of the electrode, droplet, and weld pool forms a moving inner boundary condition for the arc region. VOF Eq. (19) is solved in the metal domain to track the moving free surface with free boundary conditions set at the metal free surface. Additional body force source terms are added to the momentum transport equations at the metal free surface to consider the effects of surface tension, Maragoni shear stress, arc plasma

Table 1 Boundary conditions on the outer boundaries

	AB	BC	CD	DE	EF	FG	GA
u	0	0	0	$\frac{\partial(\rho u)}{\partial r}=0$	0	0	0
v	v_w	Eq. (25)	$\frac{\partial(\rho v)}{\partial z}=0$	0	0	0	$\frac{\partial v}{\partial r}=0$
h	$T=300$ K	$T=300$ K	$T=300$ K	$T=300$ K	$T=300$ K	$T=300$ K	$\frac{\partial T}{\partial r}=0$
ϕ	$-\sigma\frac{\partial \phi}{\partial z}=\frac{I}{\pi R_c^2}$	$\frac{\partial \phi}{\partial z}=0$	$\frac{\partial \phi}{\partial z}=0$	$\frac{\partial \phi}{\partial r}=0$	$\phi=0$	$\phi=0$	$\frac{\partial \phi}{\partial r}=0$

shear stress, and arc pressure. Additional source terms described in Eqs. (13) and (17) are added to the energy equation for the special treatment of the anode sheath and the cathode sheath.

A fixed computational domain is used to solve the equations in the arc region. The metal region is used as the inner boundary for the arc region. As the velocity of the metal domain is much smaller than the velocity of the arc plasma, the metal region serves as an inner obstacle in the arc domain. The temperature at the metal free surface is considered as the temperature boundary for the arc domain. Additional source terms described in Eqs. (16) and (18) are added to the energy equation for the arc near the anode and cathode.

3 Numerical Considerations

In the present study, the transport phenomena in the arc plasma and the metal are calculated separately in the corresponding metal domain and arc domain, and the two domains are coupled through interfacial boundary conditions in each time step. The current distribution is greatly influenced by the temperature in the arc column and the shape of the metal domain, but it is only slightly influenced by the temperature distribution in the metal domain as the electrical conductivity of metal varies slightly with temperature. Therefore, the current continuity equation and its associated boundary conditions are solved in the entire domain, while other primary variables, including p, u, v, and T, are calculated separately in the metal domain and the arc domain. The current continuity equation is iterated with the transport equations in the arc domain to obtain the current density distribution for both the arc domain and the metal domain. Iterations are required to assure convergence of each domain and then the boundary conditions are calculated from each domain for the coupling between the two domains.

For the metal domain, the method developed by Torrey et al. [40] was used to solve p, u, v, and T. This method is Eulerian and allows for an arbitrary number of segments of free surface with any reasonable shape. The basic procedure for advancing the solution through one time step, Δt, consists of three steps. First, at the beginning of the time step, explicit approximations to the momentum equations (2) and (3) are used to find provisional values of the new time velocities. Second, an iterative procedure is used to solve for the advanced time pressure and velocity fields that satisfy Eq. (1) to within a convergence criterion at the new time. Third, the energy equation is solved.

For the arc plasma domain, a fully implicit formulation is used for the time-dependent terms, and the combined convection/diffusion coefficients are evaluated using an upwind scheme. The SIMPLE algorithm [44] is applied to solve the momentum and continuity equations to obtain the velocity field. At each time step, the current continuity equation is solved first, based on the updated parameters. Current density and electromagnetic force are then calculated for the momentum and energy equations. The momentum equations and the continuity equation are then solved in the iteration process to obtain pressure and velocity. The energy equation is solved to get the new temperature distribution. Next, the temperature-dependent parameters are updated, and the program goes back to the first step to calculate the current continuity equation. This process is repeated for each time step until the convergence criteria are satisfied.

The governing differential equations (Eqs. (1)–(5) and Eq. (19)) and all related supplemental and boundary conditions are solved through the following iterative scheme:

1. At $t=0$, the electrode is set up at an initial position and initial temperature distribution is given to the metal domain. Based on the initial fixed metal domain and temperature distribution, the initial distribution of temperature, velocity, pressure, and current are obtained by solving the steady state equations in the arc domain (this procedure is similar to the steps from 5–7 for the steady state).
2. Surface tension, Marangoni shear stress, electromagnetic force, plasma shear stress, and arc pressure are calculated, and other associated boundary conditions are evaluated for the metal domain.
3. Equations (1)–(4) are solved iteratively to obtain pressure, velocity and temperature in the metal domain.
4. VOF Eq. (19) is solved to obtain the new free surface profile for the metal domain. The physical properties of cells and the boundary conditions within the computing domain are updated.
5. The current continuity equation, Eq. (5), is solved in the whole domain with updated parameters. Current density and electromagnetic force are calculated.
6. Equations (1)–(3) and the associated boundary conditions are solved iteratively to get the velocity and pressure distributions of the arc plasma. When solving these equations, the electrode, droplet and the workpiece are treated as fixed inner obstacles.
7. Energy equation, Eq. (4), is solved in the arc domain to get the new temperature distribution. Thermal physical properties of the arc plasma are updated. From here, the iteration goes back to step 5 to repeat the process for new distribution of current density, velocity pressure and temperature, until convergence criteria are satisfied.
8. Advance to the next time step and back to step 2 until the desired time is reached.

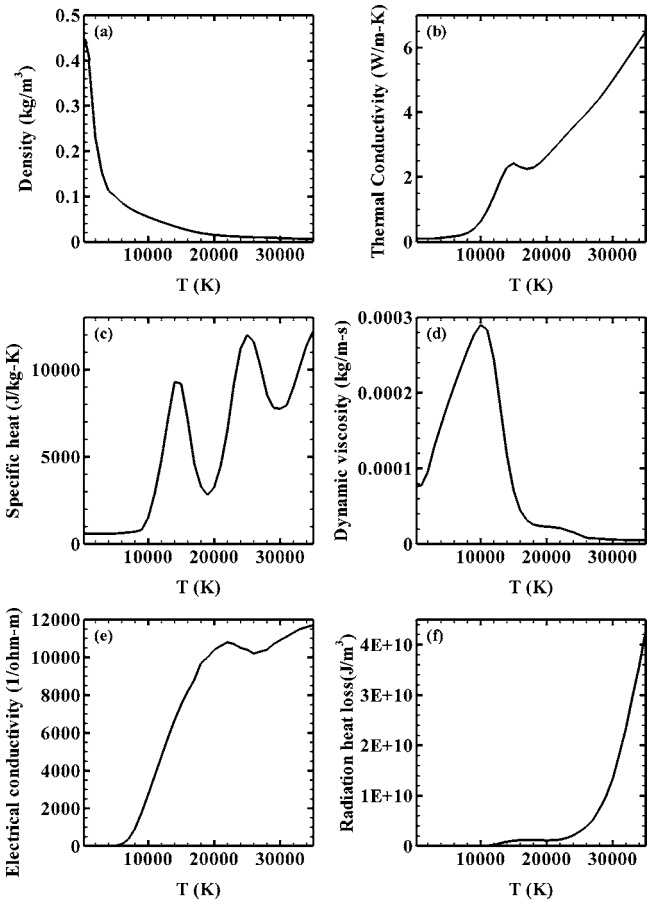

Fig. 2 Temperature-dependant material properties of argon and the volume radiation heat loss taken from [10]

A nonuniform grid point system is employed with finer grid sizes near both the cathode and anode regions. The mesh sizes near the anode and cathode center are set as 0.01 cm. Extensive tests using different grid sizes and time step sizes have been conducted to assure consistent results, and the final grid and time step sizes used can be considered the compromised between computational time and numerical accuracy. The calculation domain is half of the cylinder of 5.0 cm radius and 3.04 cm in length. Time step size is set as 5×10^{-6} s.

4 Results and Discussion

The electrode is mild steel with a 0.16 cm diameter. The workpiece is also a mild steel disk with a 3 cm diameter and a 0.5 cm thickness. The shielding gas is argon and flows out of a 1.91 cm gas nozzle at a rate of 24 l/min. The contact tube is set flush with the bottom of the gas nozzle and is 2.54 cm above the workpiece. The initial arc length is set as 0.8 cm. Five cases are studied in this paper and the current for each case is set to a constant during the calculation. Temperature-dependant material properties of argon and the volume radiation heat loss are taken from [10] and drawn in Fig. 2. The thermophysical properties of the solid and liquid mild steel are taken from [21], and are listed in Table 2 with other parameters used in the computation.

Five current levels in the range of 200–280 A, with 20 A increases, are chosen to study the effects of current on droplet formation, detachment, and acceleration in the arc. Current is a very important factor which influences the droplet formation time, size, droplet impingement velocity onto the weld pool, and thus weld pool size and penetration. Many researchers [10,21,30,31] have investigated the weld pool dynamics by assuming the droplet size,

Table 2 Thermophysical properties of mild steel and other parameters

Nomenclature	Symbol	Value (unit)
Constant in Eq. (14)	A_v	2.52
Specific heat of solid phase	c_s	700 (J kg^{-1} K^{-1})
Specific heat of liquid phase	c_l	780 (J kg^{-1} K^{-1})
Thermal conductivity of solid phase	k_s	22 (W m^{-1} K^{-1})
Thermal conductivity of liquid phase	k_l	22 (W m^{-1} K^{-1})
Density of solid phase	ρ_s	7200 (kg m^{-3})
Density of liquid phase	ρ_l	7200 (kg m^{-3})
Thermal expansion coefficient	β_T	4.95×10^{-5}(K^{-1})
Radiation emissivity	ε	0.4
Dynamic viscosity	μ_l	0.006 (kg m^{-1} s^{-1})
Latent heat of fusion	H	2.47×10^5 (J kg^{-1})
Latent heat of vaporization	H_{ev}	7.34×10^6 (J kg^{-1})
Solidus temperature	T_s	1750 (K)
Liquidus temperature	T_l	1800 (K)
Vaporization temperature	T_{ev}	3080(K)
Ambient temperature	T_∞	300 (K)
Surface tension coefficient	γ	1.2 (N m^{-1})
Surface tension temperature gradient	$\partial\gamma/\partial T$	10^{-4} (N m^{-1} K^{-1})
Electrical conductivity	σ_e	7.7×10^5 (Ω^{-1} m^{-1})
Magnetic permeability	μ_0	1.26×10^{-6} (H m^{-1})
Work function	ϕ_ω	4.3(V)
Argon ionization energy	V_i	15.76 (V)

the impingement frequency, and velocity because there is little understanding of the metal transfer process. The direct and accurate measurement of droplet velocity and acceleration is also difficult to conduct due to the complicated welding process of high speed and high temperature arc plasma. A unified model which simulates the heat transfer and fluid flow in both the droplet and arc plasma and their interaction can provide insights into how the current influences the metal transfer process. For each of the five current levels, the temperature, velocity, arc pressure, and current density distributions are obtained by solving Eqs. (1)–(7), but only a full set of data is drawn for the current level of 200 A in Figs. 3–8. The temperature and velocity distributions in the metal domain are shown in Figs. 3 and 4, respectively. The arc plasma temperature, velocity, and pressure distributions are drawn in Figs. 5–7 and current density distributions are drawn in Fig. 9 with the results for two other current levels.

The solid electrode tip is melted by the heat flux from the surrounding high temperature arc and the melted metal forms a

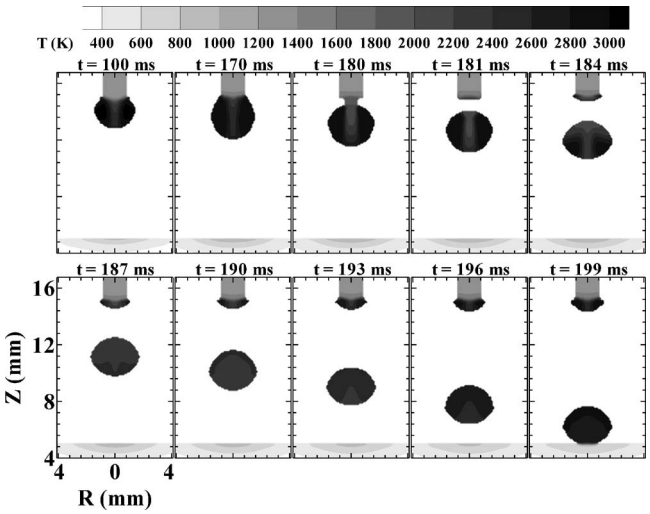

Fig. 3 Temperature distributions in the metal domain for *I* =200 A

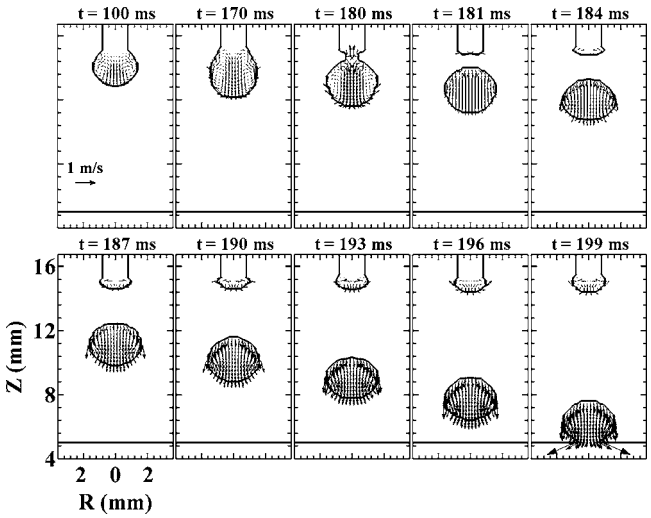

Fig. 4 Velocity distributions in the metal domain for *I*=200 A

droplet at the electrode tip under the influence of surface tension. The droplet is subjected to electromagnetic force, gravity, arc pressure, plasma shear stress, and surface tension. Arc pressure at the bottom of the droplet and surface tension are attaching forces which sustain the droplet at the electrode tip. The gravity and plasma shear stress are detaching forces which separate the droplet from the electrode tip. The radial component of the electromagnetic force has a pinch effect on the droplet and thus it is a detaching force. In argon shielded gas metal arc welding, the axial component of the electromagnetic force is also a detaching force [45]. Arc plasma has been observed to cover the entire droplet for current above 140 A [10]. From the arc coverage around the droplet, the current is hypothesized by researchers [5,10,45] to flow outside from the entire droplet surface. The radially outward current flow causes a downward detaching electromagnetic force in the droplet. The model in this paper includes the heat effect of the anode sheath and predicts a wider spread of the arc root at the droplet surface than the previous models did [22,23,32]. As seen in Fig. 5, the high temperature arc covers almost the entire droplet

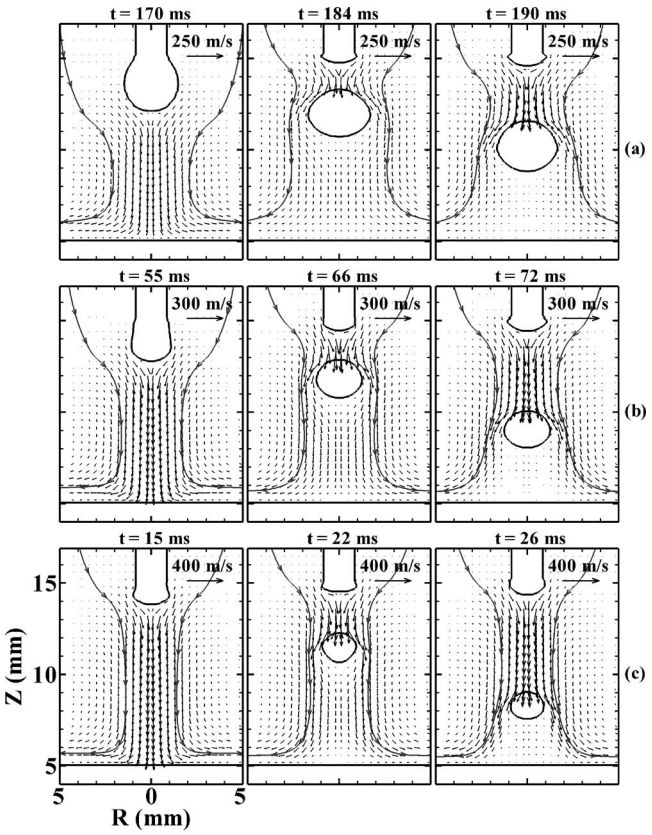

Fig. 6 Arc plasma velocity distributions for (*a*) *I*=200 A, (*b*) *I*=240 A, (*c*) *I*=280 A

surface and the current flows outward. However, compared with that of the radial component of the electromagnetic force, the detaching effect of the axial component of the electromagnetic force is small, as the current is almost parallel to the axis and only flows slightly outward. At the balance of these attaching and detaching forces, the droplet grows bigger at the electrode tip with

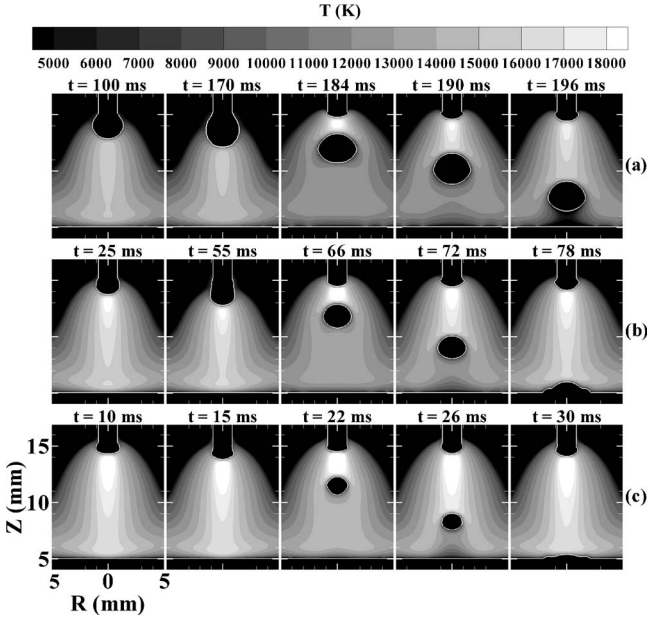

Fig. 5 Arc plasma temperature distributions for (*a*) *I*=200 A, (*b*) *I*=240 A, (*c*) *I*=280 A

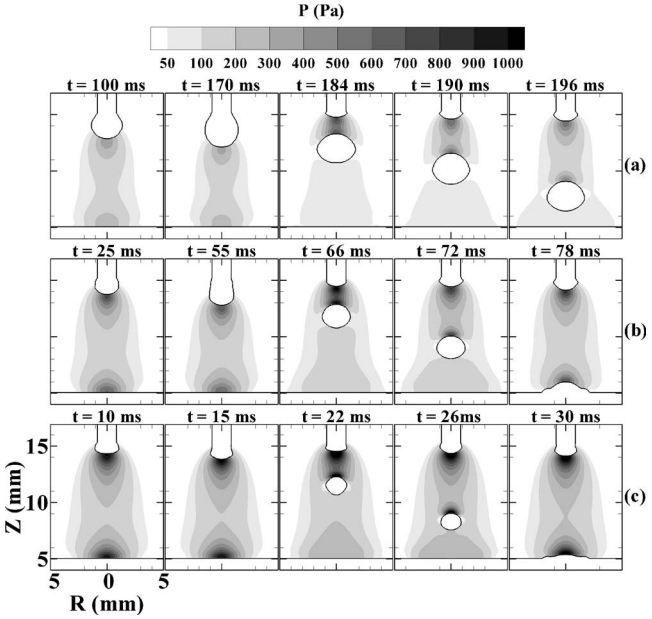

Fig. 7 Arc pressure distributions for (*a*) *I*=200 A, (*b*) *I*=240 A, (*c*) *I*=280 A

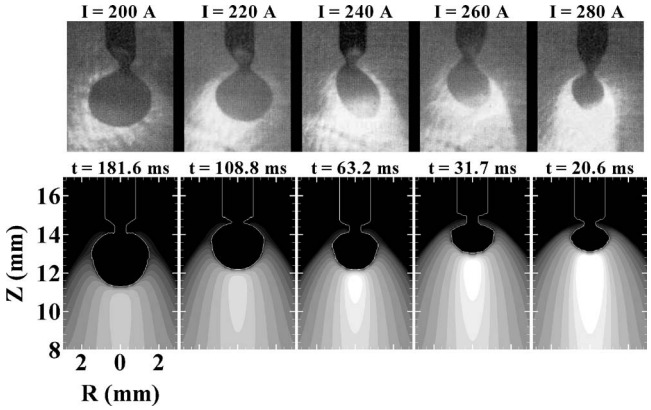

Fig. 8 Comparison of experimental results (the first row) and computational results (the second row) for droplets at the moment before detachment

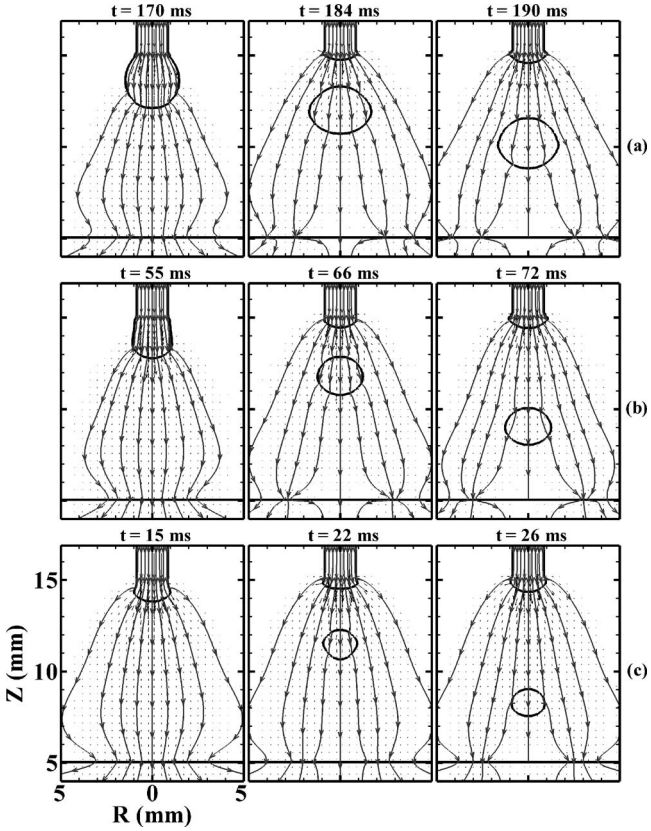

Fig. 9 Current density distributions for (*a*) *I*=200 A, (*b*) *I* =240 A, (*c*) *I*=280 A

complex flows formed inside the droplet as seen in the velocity distributions of Fig. 4. When the droplet is growing bigger, the arc pressure and surface tension becomes smaller. The droplet is detached from the electrode tip when the sustaining forces are no longer able to hold the increasing weight of the droplet. Assuming a constant surface tension coefficient in this model, the surface tension is only determined by the curvature of the droplet. Therefore, among the forces the droplet is subjected to, the changes of current will only affect the electromagnetic force, arc pressure, and plasma shear stress.

A higher current induces a higher magnetic field and thus a bigger electromagnetic force in both the metal and the arc. The bigger electromagnetic force in the arc causes a stronger arc plasma flow. As can be seen in Fig. 6, the velocity in the arc plasma becomes bigger when current increases. From Fig. 7, it can also be seen that a higher arc pressure field is formed at the electrode tip for a higher current. The bigger arc plasma velocity can also lead to a bigger plasma shear stress at the droplet surface. As the arc plasma flow is mainly drawn to the bottom of the droplet, the velocity at the arc plasma around the droplet is small. Thus, the detaching effect of the plasma shear stress is not very significant on the droplet, except at high current levels. The detaching electromagnetic force in the droplet increases faster than the attaching arc pressure with current, thus, smaller droplets are formed and detached from the electrode tip. As can be seen in Figs. 5–7, the droplet size is smaller when the current increases from 200 A to 280 A. The droplets at the moment of detachment are also compared with the experimental results of Jones et al. [4–6] in Fig. 8. It can be seen that the simulated droplet size and arc distribution around the droplet are in fair agreement with the experimental results. Only the first droplet is drawn in all the figures. However, it still can be seen that the droplet formation time is less for higher currents. As listed in Table 3, the droplet frequency obtained from several droplet formation intervals increases with higher currents. The temperature in the droplet is high near the bottom surface surrounded by the arc and low at the center where cool metal flows down from the droplet root. The temperature of the droplet only increases slightly with the current, which is mainly due to the metal evaporation effect considered in the model.

After the droplet is detached, the temperature distribution in the droplet becomes more uniform through the mixing of fluid flow inside the droplet at the beginning of the separation. The detached droplet is then heated by the surrounding high temperature arc. The detached droplet is also subjected to the electromagnetic force, gravity, arc pressure, plasma shear stress, and surface tension. At the balance of these forces, the droplet is accelerated to the workpiece. These forces are also responsible for the shape change of the droplet during the flight in the arc. The arc pressure is higher at the top surface of the detached droplet than at its bottom surface. The pressure difference does not cause the droplet to be flattened, because of the effect of surface tension, which tries to maintain a round droplet shape. The oscillation of droplet shape from oblate to prolate is mainly the work of surface tension. However, the electromagnetic force also helps the droplet to resist

Table 3 Comparison of the droplet size, frequency, and acceleration at different current levels[a]

Current (A)	Wire feed rate (cm/s)	Droplet radius (mm)	Droplet frequency (Hz)	Droplet acceleration (m/s^2)
200	4.0 (3.8)	1.49 (1.47)	5.5 (5.0)	20.6 (21.0)
220	4.5 (4.3)	1.32 (1.34)	9.2 (8.8)	25.0 (22.4)
240	5.0 (4.8)	1.13 (1.17)	16.8 (13.8)	30.4 (24.5)
260	5.5 (5.3)	0.95 (0.97)	31.5 (23.8)	38.0 (43.8)
280	6.0 (5.8)	0.82 (0.81)	65.0 (59.0)	52.4 (55.8)

[a]The experimental results shown in the parentheses are from Jones et al. [6]. The experiment was a continuous constant current welding for the 1.6 mm mild steel electrode shielded by Ar-2% O_2. The shielding gas flow rate was 24 l/min and the inner diameter of the nozzle was 19.1 mm. The contacted tube was mounted flush with the bottom of the gas nozzle and was 25.4 mm above the workpiece.

being flattened to oblate by the arc pressure. From the current streamlines drawn in Figs. 9, it can be seen that current flows around the detached droplet. Except at the place where the droplet is close to the electrode tip, only a small amount of current flows through the detached droplet. When the droplet moves farther away from the electrode tip, less current flows through it and the electromagnetic force in the droplet also becomes smaller. As it is seen in Figs. 5–7, the detached droplets have a more flattened shape near the workpiece than when they are near the electrode tip. At higher currents of 260 A and 280 A, the higher electromagnetic pinch force even elongates the detached droplets when they are near the electrode tip.

The arc pressure difference between the top and bottom surfaces of the detached droplet propels the droplet down to the workpiece. The effect of the plasma shear stress is also remarkable in bringing down the detached droplet. From the plasma velocity distributions in Fig. 6, it can be seen that the plasma flow around the detached droplet is significant. At higher currents, the plasma flow around the droplet is stronger and the arc pressure difference between the top and bottom surfaces of the droplet is greater. Therefore, a stronger acceleration of the detached droplet is found with a higher current. As shown in Figs. 5–7, the detached droplet at higher current level takes less time to reach the workpiece.

The acceleration of the droplet is found to be near constant by Jones et al. [6] and assumed to be constant by many authors in their calculations [10,21,30,31]. Jones et al. [6] have taken video images of droplets from the moment they were detached to the time they contacted the workpiece. Taken from the video images, the center positions of the droplets were then drawn with time as the flight trajectories. It was found that the flight trajectories could be fitted with quadratic curves within error limits. The first derivatives of these fitted curves were taken as the droplet velocities and the second derivatives were taken as the droplet accelerations. The droplet center positions from the computational results are compared with the fitted curves of the flight trajectories of Jones et al. [6] at each current level in Fig. 10(*a*). The solid lines are the fitted curves of the droplet trajectories from Jones et al. [6] and the symbols are the center positions of droplets from the computation. As can be seen, the calculated droplet center positions match the fitted curve well, except at some points near the electrode tip. The computational results show the droplets have a bigger acceleration at the early stage of the flight when they are near the electrode tip. While this bigger acceleration could not be shown in the fitted curve, as a constant acceleration was assumed, it was shown in the original flight trajectories made from the video images [6]. The bigger acceleration can also be explained by the computational results. From Figs. 6 and 7, it can be seen that the plasma flow between the electrode tip and the droplet is stronger and the arc pressure at the top surface of the droplet is higher when the distances between them are shorter. From the axial velocity distributions at the droplet center, which is drawn in Fig. 10(*b*) with only symbols, the trend of higher acceleration at the early stage is more obvious. The droplet velocities calculated by taking the first derivatives from both the fitted curves of the experimental and computational trajectories are drawn in Fig. 10(*b*). The droplet velocities calculated from the experimental trajectories are drawn with a solid line for each current level. The droplet velocities calculated from the computational trajectories are drawn with a dotted line and the symbol for each current level. The droplet velocities calculated from the trajectories match well for each current level. However, the velocities at the droplet center from the computational results do not fit well with them, especially at higher current levels. This is because the acceleration of the droplet is higher at the early stage. The droplet size, frequency and acceleration at different current levels are summarized in Table 3 with the corresponding experimental results.

Shielding gas flow rate is very important for the gas metal arc welding process. The flow rate should be high enough for the shielding gas to protect the weld pool, but it can not be so high that it will disturb the weld pool. A constant shielding gas flow rate is used in the computations for all the current levels. The effect of the current changes on the requirement of shielding gas flow rate is demonstrated in Fig. 6. The streamlines in all the figures start from the same point at the entrance of the shielding gas. As can be seen clearly, the streamlines are drawn more toward the center when the current increases. A higher shielding gas flow rate is required to protect the weld pool for a higher current, which is supported by the Welding Handbook [2]. However, the shielding gas can still cover the weld pool for all the current levels as the current range is not very wide in this computation.

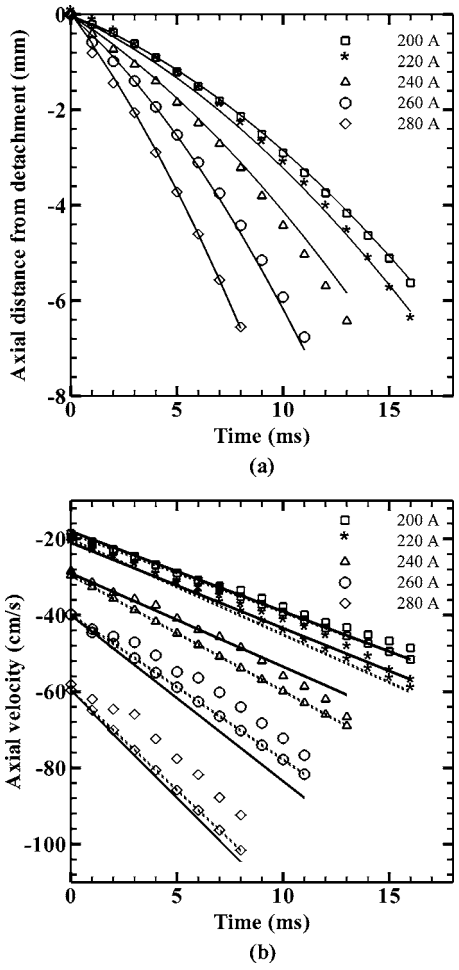

Fig. 10 Computational droplet positions and axial velocities compared with the experimental results at different currents. (*a*) Droplet flight trajectories; (*b*) axial droplet velocities.

5 Conclusions

A unified model has been used to study the droplet formation, detachment, and transfer in the arc during a gas metal arc welding process. Five current levels in the range of the globular transfer mode have been used to study the current effect on the droplet size, temperature, and acceleration. Smaller droplet size, and thus higher frequency, was found for higher currents. The temperature of the droplet at higher currents was found to be only slightly higher than at lower currents. The detached droplet was further heated by the high temperature arc during the flight in the arc. The shape of the detached droplet changes in the arc at the balance of electromagnetic force, arc pressure, plasma shear stress, and surface tension. More flattened droplets were found near the workpiece than near the electrode tip, due to the smaller electromag-

netic force further away from the electrode tip. The acceleration of the detached droplets was higher at the early stage of the flight and was near constant at the later stage. Higher acceleration was found for higher currents. The higher plasma flow driven by the electromagnetic force at higher current also showed that higher shielding flow rates were required to cover the weld pool at higher currents. The calculated results were compared with the experimental results and agreement was found.

Acknowledgment

This work was partially supported by GM R&D Center which is gratefully acknowledged.

Nomenclature

A_v = constant, defined in Eq. (14)
B_θ = self-induced azimuthal magnetic field
c = specific heat
C = coefficient, defined in Eq. (11)
c_1 = permeability coefficient, defined in Eq. (10)
d = dendrite arm spacing
e = electronic charge
F = volume of fluid function
f = mass fraction
g = volume fraction or gravitational acceleration
h = enthalpy
h_c = convective heat-transfer coefficient between the base metal and its surroundings
H = latent heat of fusion
H_{ev} = latent heat of vaporization
I = welding current
J_e = electron current density
J_i = ion current density
J_r = radial current density
J_R = current density due to electron emission
J_z = axial current density
k = thermal conductivity
K = permeability, defined in Eq. (10)
k_b = Stefan-Boltzmann constant
k_{eff} = effective thermal conductivity at arc-metal interface
m_e = electron mass
m_i = ion mass
$\boldsymbol{n}$ = vector normal to the local free surface
$n_{e,s}$ = electron number density at the sheath edge
p = pressure
P_{atm} = atmospheric pressure
p_s = surface tension pressure
Q = shielding gas flow rate
q_{ev} = evaporation mass rate of metal vapor
r-z = cylindrical coordinate system
R = gas constant
R_n = internal radius of the shielding gas nozzle
R_w = radius of the electrode
$\boldsymbol{s}$ = vector tangential to the local free surface
S_a = anode sheath energy heat flux for the metal
S_{ap} = anode sheath energy heat flux for the arc plasma
S_c = cathode sheath energy heat flux for the metal
S_{cp} = cathode sheath energy heat flux for the arc plasma
S_R = radiation heat loss
t = time
T = temperature
T_{arc} = arc plasma temperature close to the anode and cathode
T_a, T_c = anode, cathode surface temperature
$T_{e,s}$ = electron temperature at the sheath edge
T_l = liquidus temperature
T_s = solidus temperature
T_∞ = ambient temperature
u = velocity in the r direction
v = velocity in the z direction
$\boldsymbol{V}$ = velocity vector
v_B = Bohm velocity
V_i = ionization energy of plasma
V_s = anode sheath voltage drop
$\boldsymbol{V}_r$ = relative velocity vector $(\boldsymbol{V}_l - \boldsymbol{V}_s)$
V_w = wire feed rate

Greek Symbols

β_T = thermal expansion coefficient
γ = surface tension coefficient
$\partial\gamma/\partial T$ = surface tension temperature gradient
ε = surface radiation emissivity
κ = free surface curvature
μ_l = dynamic viscosity
μ_0 = magnetic permeability
ϕ = electric potential
ϕ_w = work function of the anode material
σ_e = electrical conductivity
ρ = density
τ_{ps} = plasma shear stress
τ_{Ms} = Marangoni shear stress
δ = mesh size near the anode or cathode sheath surface
Δt = time interval

Subscripts

0 = initial value
l = liquid phase
r = relative to solid phase velocity
s = solid phase
w = wire

References

[1] Kim, C. H., Zhang, W., and DebRoy, T., 2003, "Modeling of Temperature Field and Solidified Surface Profile During Gas-Metal Arc Fillet Welding," J. Appl. Phys., **94**, pp. 2667–2679.
[2] AWS, 1983, *Welding Handbook*, 7th ed., American Welding Society, Vol. 2.
[3] Lin, Q., Li, X., and Simpson, S. W., 2001, "Metal Transfer Measurements in Gas Metal Arc Welding," J. Phys. D, **34**, pp. 347–353.
[4] Jones, L. A., Eagar, T. W., and Lang, J. H., 1998, "Images of Steel Electrode in Ar-2%O_2 Shielding during Constant Current Gas Metal Arc Welding," Weld. J. (Miami, FL, U.S.), **77**, pp. 135–141s.
[5] Jones, L. A., Eagar, T. W., and Lang, J. H., 1998, "Magnetic Forces Acting on Molten Drops in Gas Metal Arc Welding," J. Phys. D, **31**, pp. 93–106.
[6] Jones, L. A., Eagar, T. W., and Lang, J. H., 1998, "A Dynamic Model of Drops Detaching from a Gas Metal Arc Welding Electrode," J. Phys. D, **31**, pp. 107–123.
[7] Simpson, S. W., and Zhu, P. Y., 1995, "Formation of Molten Droplets at a Consumable Anode in an Electric Welding Arc," J. Phys. D, **28**, pp. 1594–1600.
[8] Nemchinsky, V. A., 1994, "Size and Shape of the Liquid Droplet at the Molten Tip of an Arc Electrode," J. Phys. D, **27**, pp. 1433–1442.
[9] Choi, J. H., Lee, J., and Yoo, C. D., 2001, "Dynamic Force Balance Model for Metal Transfer Analysis in Arc Welding," J. Phys. D, **34**, pp. 2658–2664.
[10] Lancaster, J. F., 1986, *The Physics of Welding*, 2nd ed., Pergamon, Oxford.
[11] Zhang, Y. M., and Liguo, E., 2000, "Numerical Analysis of the Dynamic Growth of Droplets in Gas Metal Arc Welding," Proc. Inst. Mech. Eng., Part C: J. Mech. Eng. Sci., **214** Part C, pp. 1247–1258.
[12] Zhang, Y. M., and Li, P. J., 2001, "Modified Active Control of Metal Transfer and Pulsed GMAW of Titanium," Weld. J. (Miami, FL, U.S.), **80**, pp. 54–61s.
[13] Fan, H. G., and Kovacevic, R., 1998, "Dynamic Analysis of Globular Metal Transfer in Gas Metal Arc Welding: A Comparison of Numerical and Experimental Results," J. Phys. D, **31**, pp. 2929–2941.
[14] Choi, S. K., Yoo, C. D., and Kim, Y. S., 1998, "The Dynamic Analysis of Metal Transfer in Pulsed Current Gas Metal Arc Welding," J. Phys. D, **31**, pp. 207–215.
[15] Choi, S. K., Kim, Y. S., and Yoo, C. D., 1999, Dimensional Analysis of Metal Transfer in GMA Welding," J. Phys. D, **32**, pp. 326–334.
[16] Choi, S. K., Yoo, C. D., and Kim, Y. S., 1998, "Dynamic Simulation of Metal Transfer in GMAW, Part 1: Globular and Spray Transfer Modes," Weld. J. (Miami, FL, U.S.), **77**, pp. 38–44s.

[17] Choi, S. K., Yoo, C. D., and Kim, Y. S., 1998, "Dynamic Simulation of Metal Transfer in GMAW, Part 2: Short-Circuit Transfer Mode," Weld. J. (Miami, FL, U.S.), **77**, pp. 45–51s.
[18] Wang, G., Huang, P. G., and Zhang, Y. M., 2003, "Numerical Analysis of Metal Transfer in Gas Metal Arc Welding under Modified Pulsed Current Conditions," Metall. Mater. Trans. B, **35B**, pp. 857–866.
[19] Zhu, P., Rados, M., and Simpson, S. W., 1995, "A Theoretical Study of Gas Metal Arc Welding System," Plasma Sources Sci. Technol., **4**, pp. 495–500.
[20] Wang, F., Hou, W. K., Hu, S. J., Kannatey-Asibu, E., Schultz, W. W., and Wang, P. C., 2003, "Modelling and Analysis of Metal Transfer in Gas Metal Arc Welding," J. Phys. D, **36**, pp. 1143–1152.
[21] Fan, H. G., and Kovacevic, R., 1999, "Droplet Formation, Detachment, and Impingement on the Molten Pool in Gas Metal Arc Welding," Metall. Mater. Trans. B, **30B**, pp. 791–801.
[22] Haidar, J., and Lowke, J. J., 1996, "Predictions of Metal Droplet Formation in Arc Welding," J. Phys. D, **29**, pp. 2951–2960.
[23] Haidar, J., 1998, "An Analysis of the Formation of Metal Droplets in Arc Welding," J. Phys. D, **31**, pp. 1233–1244.
[24] Haidar, J., 1998, "A Theoretical Model for Gas Metal Arc Welding and Gas Tungsten Arc Welding. I," J. Appl. Phys., **84**, pp. 3518–3529.
[25] Haidar, J., 1998, "Prediction of Metal Droplet Formation in Gas Metal Arc Welding II," J. Appl. Phys., **84**, pp. 3530–3540.
[26] Haidar, J., 1998, "An Analysis of Heat Transfer and Fume Production in Gas Metal Arc Welding. III.," J. Appl. Phys., **85**, pp. 3448–3459.
[27] Zhu, F. L., Tsai, H. L., Marin, S. P., and Wang, P. C., 2004, "A Comprehensive Model on the Transport Phenomena during Gas Metal Arc Welding Process," Prog. Comput. Fluid Dyn., **4**, pp. 99–117.
[28] Fan, H. G., and Kovacevic, R., 2004, "A Unified Model of Transport Phenomena in Gas Metal Arc Welding including Electrode, Arc Plasma and Molten Pool," J. Phys. D, **37**, pp. 2531–2544.
[29] Subramaniam, S., White, D. R., Scholl, D. J., and Weber, W. H., 1998, "In Situ Optical Measurement of Liquid Drop Surface Tension in Gas Metal Arc Welding," J. Phys. D, **31**, pp. 1963–1967.
[30] Wang, Y., and Tsai, H. L., 2001, "Impingement of Filler Droplets and Weld Pool Dynamics During Gas Metal Arc Welding Process," Int. J. Heat Mass Transfer, **44**, pp. 2067–2080.
[31] Wang, Y., and Tsai, H. L., 2001, "Effects of Surface Active Elements on Weld Pool Fluid Flow and Weld Penetration in Gas Metal Arc Welding," Metall. Mater. Trans. B, **32B**, pp. 501–515.
[32] Hu, J., 2005, "Heat and Mass Transfer in the Gas Metal Arc Welding Process," Ph.D. dissertation, University of Missouri-Rolla, Rolla, MO.
[33] Chiang, K. C., and Tsai, H. L., 1992, "Shrinkage Induced Fluid Flow and Domain Change in Two-Dimensional Alloy Solidification," Int. J. Heat Mass Transfer, **35**, pp. 1763–1770.
[34] Carman, P. C., 1937, "Fluid Flow Through Granular Beds," Trans. Inst. Chem. Eng., **15**, pp. 150–166.
[35] Kubo, K., and Pehlke, R. D., 1985, "Mathematical Modeling of Porosity Formation in Solidification," Metall. Trans. A, **16A**, pp. 823–829.
[36] Beavers, G. S., and Sparrow, E. M., 1969, "Non-Darcy Flow through Fibrous Porous Media," ASME J. Appl. Mech., **36**, pp. 711–714.
[37] Lowke, J. J., Kovitya, P., and Schmidt, H. P., 1992, "Theory of Free-Burning Arc Columns Including the Influence of the Cathode," J. Phys. D, **25**, pp. 1600–1606.
[38] Zacharia, T., David, S. A., and Vitek, J. M., 1992, "Effect of Evaporation and Temperature-Dependent Material Properties on Weld Pool Development," Metall. Trans. B, **22B**, pp. 233–241.
[39] Jonsson, P. G., Westhoff, R. C., and Szekely, J., 1993, "Arc Characteristics in Gas-Metal Arc Welding of Aluminum Using Argon as the Shielding Gas," J. Appl. Phys., **74**, pp. 5997–6006.
[40] Torrey, M. D., Cloutman, L. D., Mjolsness, R. C., and Hirt, C. W., 1995, "NASA-VOF2D: A Computer Program for Incompressible Flows with Free Surfaces," LA-10612-MS, Los Alamos National Laboratory.
[41] Brackbill, J. U., Kothe, D. B., and Zemach, C., 1992, "A Continuum Method for Modeling Surface Tension," J. Comput. Phys., **100**, pp. 335–354.
[42] Celic, A., and Zilliac, G. G., 1997, "Computational Study of Surface Tension and Wall Adhesion Effects on an Oil Film Flow Underneath an Air Boundary Layer," Nasa Ames Research Center.
[43] Granger, R. A., 1995, *Fluid Mechanics*, CBS College, New York, Chap. 10.
[44] Patanka, S. V., 1980, *Numerical Heat Transfer and Fluid Flow*, McGraw-Hill, New York.
[45] Nemchinsky, V. A., 1996, "The Effect of the Type of Plasma Gas on Current Constriction at the Molten Tip of an Arc Electrode," J. Phys. D, **29**, pp. 1202–1208.